Development of high-strength WNbMoTaVZr$_x$ refractory high entropy alloys

C. Li[1], S. H. Chen[1,2,a)], Z. W. Wu[1], Z. F. Zhang[1], Y. C. Wu[2,3,a)]

[1] School of Mechanical Engineering, Hefei University of Technology, Hefei 230009, China
[2] National-Local Joint Engineering Research Centre of Nonferrous Metals and Processing Technology, Hefei 230009, China
[3] School of Materials Science and Engineering, Hefei University of Technology, Hefei 230009, China
[a)] Address all correspondence to these authors. e-mails: shchen@hfut.edu.cn; ycwu@hfut.edu.cn

In this work, novel WNbMoTaVZr$_x$ (x = 0.1, 0.25, 0.5, 0.75, 1.0) refractory high entropy alloys (RHEAs) were developed, and the corresponding phase formation, microstructure and mechanical properties were investigated. As compared with the WNbMoTa and WNbMoTaV derivative alloys, the present WNbMoTaVZr$_x$ RHEAs demonstrated significantly improved strength and hardness, especially the specific yield strength. The increase of the strength was attributed to the solid solution strengthening effect, resulting from the severe lattice distortion associated with lager-atomic-sized Zr element. With the increase of Zr content, the microstructure changed from grain morphology to dendritic structures. The formation of the second phase with the increase of Zr content was also observed, and its effects on the strengthening, plastic deformation and fracture behaviors were discussed. The deformation-evolution investigations have shown that under applied loadings, microcracks initiated at interdendritic regions with relatively soft second phase. The phase thermostability analysis suggests that the phase structure of typical WNbMoTaVZr$_x$ RHEAs could be stable at elevated temperature.

Introduction

Differing from the conventional alloys with one or two principal elements, high entropy alloys (HEAs) are known to have at least five principal elements, with equiatomic or near equiatomic ratios between 5 and 35% [1]. With specially designed compositions, four core effects were reported for HEAs, i.e., the high entropy effect, sluggish diffusion effect, severe lattice distortion effect, and cocktail effect [2–4]. Due to the high entropy effect, the alloy with multi-principal elements tends to form single solid solution structure rather than intermetallic [5–8]. Combined with the abovementioned effects, HEAs can exhibit excellent mechanical properties, such as high strength [6, 9–11], high hardness [9, 12], good oxidation resistance [13], and attractive wear resistance [14] and corrosion resistance [15, 16]. In 2010, WNbMoTa and WNbMoTaV HEAs consisting of high-melting-point elements were reported by Senkov et al. [17], exhibiting excellent mechanical properties at elevated temperature from 600 to 1600 °C. These alloys were therefore named as refractory high entropy alloys (RHEAs), which could have great potential for high temperature applications. Additionally, it is known that the W element with

high melting point was regarded as a candidate for plasma-facing materials, and the W-contained alloys could be applied in harsh working environment, such as nuclear fusion reactors [18]. Thereafter, more research attention was focused on the development and mechanical properties of W-contained RHEAs, including the WNbMoTa and WNbMoTaV derivative alloys. For example, by adding Ti element, the WNbMoTaTi and WNbMoTaVTi RHEAs demonstrated high thermal stability at 1200 °C and good room temperature mechanical properties with yield strength improved to 1343 MPa and 1515 MPa, respectively [6]. A study showed that the Ti content can significantly influence the mechanical properties of WNbMoTa RHEA. With the increase Ti content from 0 to 1, the yield strength increased form 996 MPa to 1455 MPa and fracture strains increased from 1.9% to 11.5% [19]. The WNbMoTa-Cr, WNbMoTa-Re, WNbMoTa-Hf and WNbMoTa-Zr RHEAs were also developed, demonstrating enhanced strength reaching 1056 MPa, 1062 MPa, 1252 MPa and 1480 MPa, respectively [20]. Furthermore, the influence of Re content on the mechanical properties was also studied. With the increase of Re content from 0 to 1 in mole ratio, the yield strength increased from 1121 to 1147 MPa,

and then decreased to 1062 MPa, demonstrating fracture strains of 6.2%, 7.0% and 4.2%, respectively [21]. Up to date, to enhance the strength of RHEAs is still important, especially for high temperature applications. Studies have shown that the addition of Zr element can significantly improve the mechanical properties of some HEAs [22], and the $CoCrFeNiMnZr_{0.8}$ HEA even had nearly twice yield strength as compared with the parent CoCrFeNiMn HEA. The addition of Zr can lead to solid solution strengthening due to the severe lattice distortion caused by its lager atomic size, improving the mechanical properties of HEAs [23]. Therefore, in this work, a novel $WNbMoTaVZr_x$ RHEA system was developed, which demonstrated greatly enhanced yield strength than the parent WNbMoTaV RHEA. The phase structure, microstructure, and deformation mechanisms of $WNbMoTaVZr_x$ RHEAs were examined and discussed.

Results

Phase structure of the WNbMoTaVZr$_x$ RHEAs

The X-ray diffraction (XRD) patterns of the $WNbMoTaVZr_x$ RHEAs are shown in Fig. 1. It can be seen that the VZr0.1, VZr0.25, RHEAs have single BCC solid solution phase. As reported by Zhang et al. [24], an alloy system tends to form solid solution phases when $-15 \leq \Delta H_{mix} \leq 5$ kJ mol^{-1}, $12 \leq \Delta S_{mix} \leq 17.5$ J mol^{-1} K^{-1}, and $\delta \leq 6.5\%$, where ΔH_{mix} is the enthalpy of mixing, ΔS_{mix} denotes the entropy of mixing, and δ is the atomic radius difference. These parameters can be calculated as:

$$\Delta H_{mix} = \sum_{\substack{i=1 \\ i \neq j}}^{n} 4\Delta H_{ij}c_i c_j \qquad (1)$$

$$\Delta S_{mix} = -R \cdot \sum_{i=1}^{n} (c_i \cdot \ln c_i) \qquad (2)$$

$$\delta = \sqrt{\sum_{i=1}^{n} c_i \left(1 - \frac{r_i}{\bar{r}}\right)^2} \times 100, \qquad (3)$$

where ΔH_{ij} is the enthalpy of mixing between the ith and jth elements, calculated based on the Miedema's model [25]; c_i and c_j are the atomic percentages of the ith and jth elements, respectively; $R = 8.314$ J K^{-1} mol^{-1} is the gas constant; n is the number of elements in the alloy; r_i is the atom radius of the ith element; and $\bar{r}$ is the average radius. Moreover, Guo et al. [26] reported that when the valence electron concentration (VEC) < 6.78, the alloy system tends to form body-centered cubic (BCC) phase, and when VEC > 8, the face-centered cubic (FCC) phase was preferred. The VEC of the alloy system can be obtained according to the equation:

$$VEC = \sum_{i=1}^{n} c_i (VEC)_i, \qquad (4)$$

where $(VEC)_i$ is the valence electron concentration of the ith element, and c_i is the atomic percentage of the ith element. Based on the relationship between the mixing of entropy and enthalpy, Yang et al. [27] proposed a new parameter, Ω, to predict the formation of solid solution phase, as denoted as:

$$\Omega = \frac{T_m \Delta S_{mix}}{|\Delta H_{mix}|}, \qquad (5)$$

where T_m is the average melting point of elements. Combined with δ, when $\Omega \geq 1.1$, $\delta \leq 6.6\%$, the alloy system tends to form solid solution structure. In this work, the physical properties and parameters for W, Nb, Mo, Ta, V and Zr elements are listed in Table 1. The aforementioned empirical parameters of the $WNbMoTaVZr_x$ RHEA (the alloys with $x = 0.1, 0.25, 0.5, 0.75, 1.0$ are denoted as VZr0.1, VZr0.25, VZr0.5, VZr0.75 and VZr1.0,
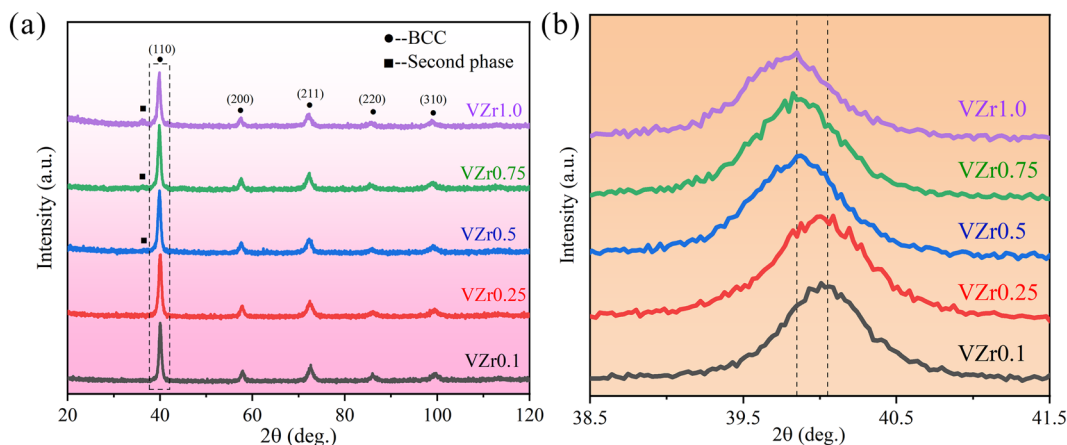

Figure 1: XRD patterns of the WNbMoTaVZr$_x$ RHEAs (a), where (b) shows the (110) peak in (a) at a higher magnification.

TABLE 1: The physical properties and parameters for each element in the WNbMoTaVZr_x RHEA system.

Element	W	Nb	Mo	Ta	V	Zr
Atomic radius (Å)	1.367	1.429	1.363	1.43	1.34	1.603
VEC	6	5	6	5	5	4
Melting point (K)	3695	2750	2896	3290	2183	2128
Lattice constant (pm)	316.5	330.1	314.7	330.3	303.0	358.2

TABLE 2: The calculated empirical parameters (entropy of mixing (ΔS_{mix}), enthalpy of mixng (ΔH_{mix}), atomic radius difference (δ), valence electron concentration (VEC), average melting point (T_m) and Ω) of WNbMoTaVZr_x (x = 0.1, 0.25, 0.5, 0.75, 1.0) RHEAs.

RHEA	ΔS_{mix} [J K^{-1} mol^{-1}]	ΔH_{mix} (kJ mol^{-1})	δ (%)	VEC	T_m (K)	Ω
VZr0.1	13.919	− 4.644	3.4	5.37	2946.5	8.83
VZr0.25	14.335	− 4.644	4.19	5.33	2923.1	9.02
VZr0.5	14.698	− 4.628	5.1	5.27	2886.8	9.17
VZr0.75	14.856	− 4.597	5.72	5.22	2853.9	9.22
VZr1.0	14.897	− 4.556	6.16	5.17	2823.8	9.23

respectively) were therefore calculated, and given in Table 2. It can be seen that all the values of empirical parameters are within the ranges as proposed, suggesting the formation of single BCC solid solution phase. However, with the increase of Zr content, the VZr0.5, VZr0.75 and VZr1.0 RHEAs also exhibited mainly single BCC solid solution phase, but a weak peak was observed besides the (110) peak, suggesting the formation of a small amount of second phase. It was reported that ΔH_{mix} and δ are the main parameters which influenced the phase stability of HEAs [3]. It can be found from Table 2 that the ΔH_{mix} values were similar for all WNbMoTaVZr_x RHEAs, while the parameter δ increased from 3.40 to 6.16 from VZr0.1 to VZr1.0 RHEAs, which indicates that the addition of more Zr resulted in severe lattice distortion. The severe lattice distortion may cause the increase of strain energy, leading to phase instability. On the other hand, with severe lattice distortion, it is more difficult for the element to diffuse, which may cause the formation of nano precipitations [28, 29]. The appearance of the second phase may be due to the increase of phase instability resulting from the increase of Zr content.

The (110) peaks of the BCC structure of RHEAs were magnified, as shown in Fig. 1(b) It can be seen that with the increase of Zr content, the (110) peak shifted towards lower 2θ angle from VZr0.1 to VZr1.0 RHEA, suggesting the increase of lattice parameter [30, 31]. The experimental values of lattice parameter ($a_{exp.}$) for the BCC and second phases of WNbMoTaVZr_x RHEAs were calculated according to the Bragg's law and XRD results. The Bragg equation is shown as:

$$2d \sin \theta = n * \lambda, \tag{6}$$

where d is interplanar spacing of crystal planes, θ is the diffraction angle of peak, n is the diffraction order which is a positive integer generally equal to 1, and λ is the wave-length of X-ray radiation (0.154056 nm). Besides, the relationship between the lattice parameter (a) and interplanar spacing (d) can be described by the following equation:

TABLE 3: Experimental ($a_{exp.}$) and theoretical ($a_{tho.}$) values of the lattice parameters for the main BCC and second phases.

RHEAs	VZr0.1	VZr0.25	VZr0.5	VZr0.75	VZr1.0
$a_{exp.}$-BCC phase (Å)	3.190	3.192	3.199	3.203	3.219
$a_{exp.}$-second phase (Å)	–	–	3.485	3.500	3.509
$a_{tho.}$ (Å)	3.197	3.208	3.225*	3.240*	3.255*

The theoretical values with stars (*) were obtained based on the assumption that only one BCC phase occurs, which were therefore only used for reference here due to the formation of the second phase for VZr0.5, VZr0.75 and VZr1.0 RHEAs.

$$a = d\sqrt{h^2 + k^2 + l^2}, \tag{7}$$

where (h, k, l) are the calculated peak's Miller indices. Equation (6) can then be revised as:

$$a_{exp.} = \lambda\sqrt{h^2 + k^2 + l^2}/2 \sin \theta \tag{8}$$

As shown in Table 3, the calculated lattice parameter of both the BCC and second phases increased with the increase of Zr content. On the other hand, the theoretical lattice parameters ($a_{tho.}$) were also calculated using the rule of mixtures according to following equation [8]:

$$a_{tho.} = \sum_{i=1}^{n} c_i a_i, \tag{9}$$

where c_i and a_i are the atomic percentage and lattice parameter of the ith element, respectively. According to Eq. (9), the increase of Zr content with lager atomic radius also leads to the increase of the lattice parameter (a). The theoretical lattice parameters show similar trend on the change of Zr content, agreeing well with the experimental results. With the increase of Zr content, the empirical parameter δ increased, resulting in larger lattice distortion and the increase of lattice parameter a. It can then be concluded that with the increase of Zr element,

Article

the RHEAs tend to have larger lattice distortion, which may also affect the mechanical performance of the RHEAs.

Microstructure of the WNbMoTaVZr$_x$ RHEAs

The typical microstructures of WNbMoTaVZr$_x$ RHEAs are shown in Fig. 2. The VZr0.1 RHEA has clear grain morphology [Fig. 2(a)], similar to the results of the WNbMoTaV RHEA [17]. However, the average grain size of VZr0.1 was calculated as 40 μm, which about is half of WNbMoTaV RHEA [17], suggesting the refinement of the grain size with the minor addition of Zr element. With further increase of Zr content, dendritic microstructures were found in VZr0.25-VZr1.0 RHEAs, similar to the results of other RHEAs [8, 32, 33]. And with the increase of Zr content, the interdendritic regions also increased. Combined with the XRD results, it can be speculated that the VZr0.1 RHEA exhibited single BCC structure similar to the parent WNbMoTaV RHEA, having grain morphology. While the second phase appeared in VZr0.25–VZr1.0 RHEAs, concentrated at interdendritic regions, where the volume fraction of the second phase increased with the addition of Zr content. For the VZr0.25 RHEA, due to the limited volume fraction of the second phase, no obvious peak for the second phase was observed. With lower Zr contents in VZr0.25 and VZr0.5 RHEAs, relatively uniform dendritic structures were formed due to the appearance of the second phase at interdendritic regions. While with the increase of Zr content in VZr0.75 and VZr1.0 RHEAs, more second phase was formed, resulting in enlarged dendritic structures and local concentrations, such as the regions indicated by the rectangles D and E in Fig. 2(d) and (e). By

use of the Image J software, the volume fractions of the second phase at interdendritic regions were calculated based on the SEM images, and the results are shown in Table 4. It can be seen that with the addition of more Zr content, the volume fraction of the second phase also increased significantly, and reached 13.75% in the VZr1.0 RHEA.

In order to differentiate the variation of elements between the BCC phase and the second phase, the microstructures of WNbMoTaVZr$_x$ RHEAs were further inspected by an Energy Dispersive Spectrometer (EDS), and the results are given in Fig. 3. It can be seen that large discrepancy in compositions was observed for the dendritic structures. The W and Ta elements with high melting points were more concentrated in dendritic regions, while the Zr and Nb and V elements were more concentrated in interdendritic regions. And there was no significant variation in the distribution of Mo between dendritic and interdendritic regions. The concentrations of elements can be ascribed to the different melting points. The W and Ta elements with high melting points could solidify firstly in dendritic regions, while the Zr, Nb and V elements with lower melting points tends to solidify later in interdendritic regions [34, 35].

TABLE 4: The volume fraction of the second phase as well as the atomic percentage of Zr element for the WNbMoTaVZr$_x$ RHEAs.

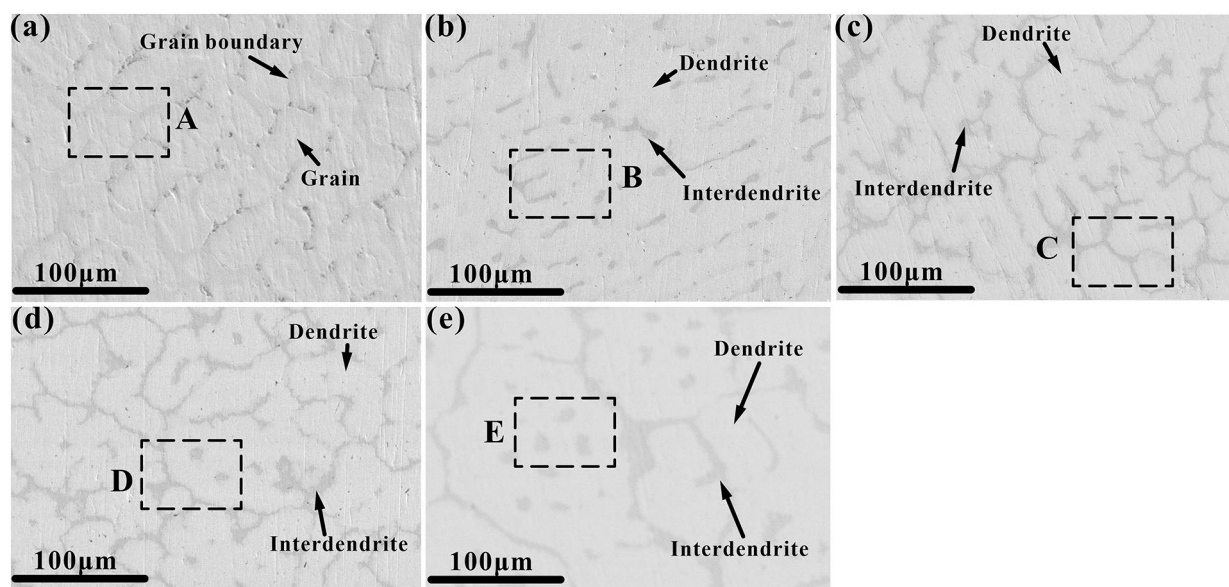| RHEAs	VZr0.1	VZr0.25	VZr0.5	VZr0.75	VZr1.0
Volume fraction of the second phase (%)	–	4.31	7.42	10.57	13.75
Atomic percentage of Zr (%)	1.96	4.76	9.09	13.04	16.67

Figure 2: SEM images showing the microstructure of the VZr0.1 (a), VZr0.25 (b), VZr0.5 (c), VZr0.75 (d) and VZr1.0 (e) RHEAs, respectively.
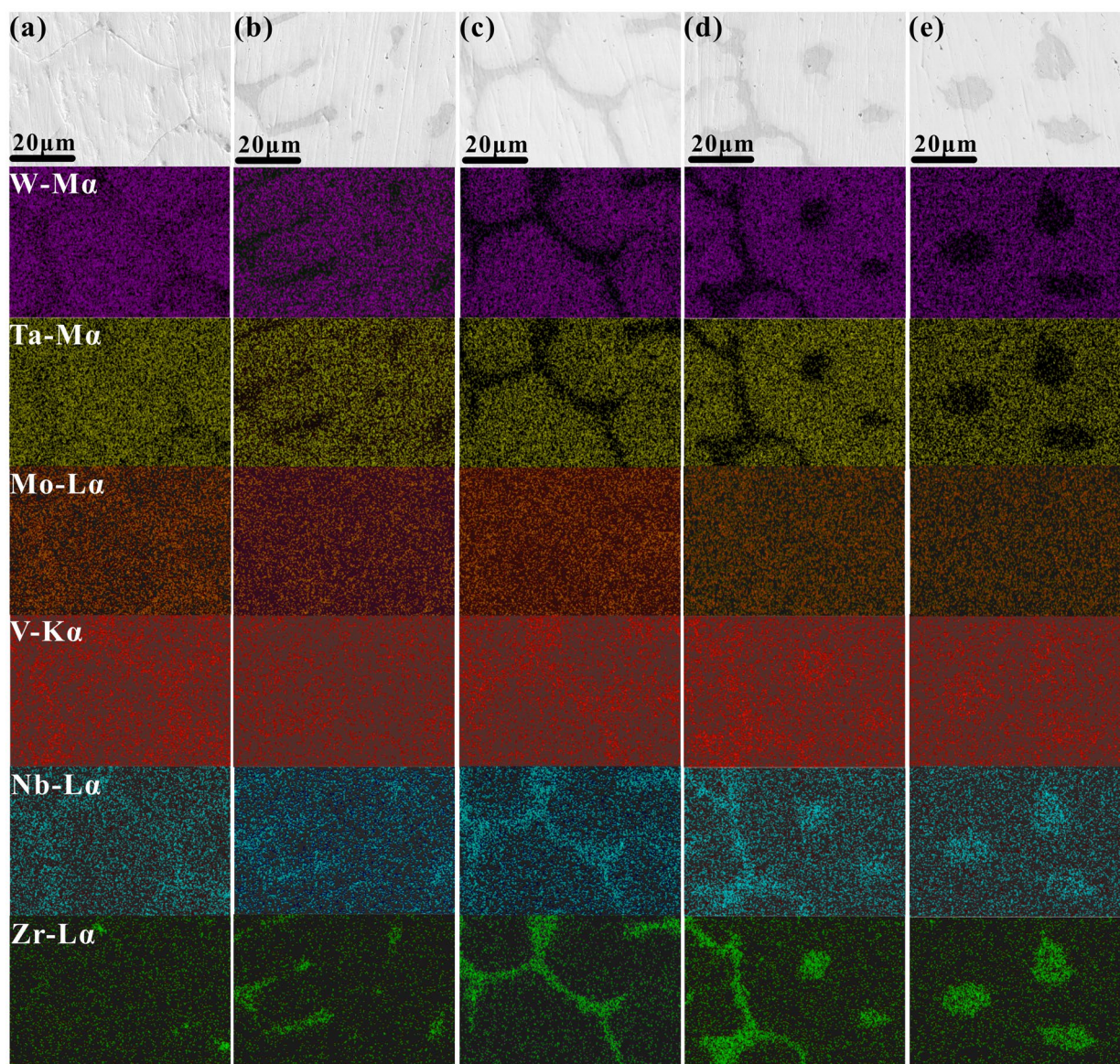
Figure 3: SEM images of the VZr0.1 (a), VZr0.25 (b), VZr0.5 (c), VZr0.75 (d) and VZr1.0 (e) RHEAs at a higher magnification, as indicated by the rectangles A-E in Fig. 2. The corresponding EDS mapping results of W, Ta, Mo, V, Nb and Zr elements were also given below.

To further verify the crystal structure of the main BCC phase and the second phase, typical VZr0.5 and VZr1.0 RHEAs were examined by transmission electron microscopy (TEM). The TEM results have confirmed the BCC structure of dendritic regions, and the second phase at interdendritic regions also has BCC structure. To differentiate the two phases, the main BCC phase in dendritic regions was noted as BCC1 phase, and the second BCC phase at interdendritic regions was noted as BCC2 phase in the following sections. As shown in Fig. 4(a) and (b), the regions for BCC1 and BCC2 phases were determined according to the EDS results, where the BCC1 regions were enriched with W and Ta elements while the BCC2 regions were enriched with Zr and Nb elements. The select area electron diffraction (SAED) patterns, showing the

BCC structure of both dendritic and interdendritic regions, are also given in Fig. 4. Based on the SAED patterns, the lattice parameters of the BCC1 phase were 3.20 Å and 3.26 Å for VZr0.5 and VZr1.0 RHEAs, respectively. The lattice parameters of the BCC2 phase were 3.51 Å and 3.53 Å for VZr0.5 and VZr1.0 RHEAs, respectively. With the increase of Zr content, the lattice parameters also increased, and the lattice parameter results agree well with the XRD results as shown in Table 3.

Mechanical properties of the WNbMoTaVZr$_x$ RHEAs

The representative compressive engineering stress–strain curves are shown in Fig. 5(a). The corresponding mechanical properties, such as the yield strength (σ_y), the maximum
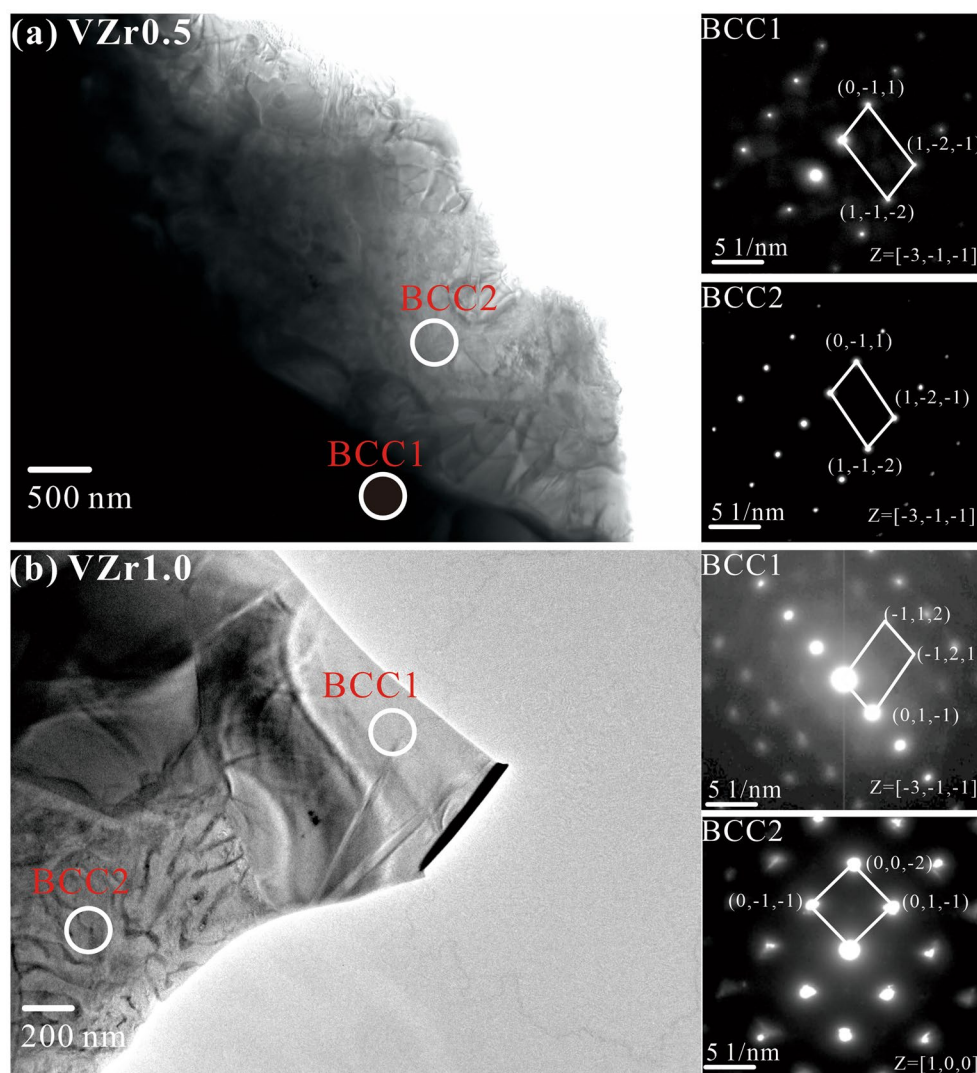
Figure 4: Bright field TEM images of the VZr0.5 (a) and VZr1.0 (b) RHEAs as well as the corresponding SAED patterns. The sites for BCC1 and BCC2 phases correspond to dendritic and interdendritic regions, respectively.

compressive strength (σ_m), and the fracture strain (ε_f), are listed in Table 5. As compared with the WNbMoTaV HREA, having a yield strength (σ_y) of about 1246 MPa, a maximum strength (σ_m) of about 1270 MPa and a fracture strain (ε_f) of about 1.7%, the WNbMoTaVZr$_x$ RHEAs have significantly enhanced yield strength and maximum strength. And overall these two values increased with the increase of Zr content, reaching maximum values of 1680 MPa (σ_y) and 1919 MPa (σ_m), respectively. The Vicker hardness of the WNbMoTaVZrx RHEAs also increased significantly, as shown in Fig. 5(b). For example, the average value increased from 525 kgf mm^{-2} in WNbMoTaV HREA to 595 kgf mm^{-2} in the VZr1.0 RHEA. However, with the increase of the Zr content, no obvious increase of hardness was observed. The increase of the strength of the RHEAs with the addition of more Zr content

can be attributed to the solid solution strengthening effect, resulting from the severe lattice distortion caused by larger Zr atom radius size [6, 36, 37]. Moreover, the increase of the yield strength of the VZr1.0 RHEA is relatively smaller as compared with VZr0.1–VZr0.75 RHEAs. The average maximum strength of the VZr1.0 RHEA is even slightly smaller than the value of the VZr0.75 RHEA. Regarding the formation of BCC2 phase, if the present RHEAs were simplified as a quasi-binary alloy system, the increasement of the yield strength, related to the concentration of Zr, can be expressed as the equation [5]:

$$\Delta\sigma \propto c^n, \tag{10}$$

where n is a material parameter ranging from 1/3 to 1, which was chosen as 0.5 similar to other conventional alloys. The parameter $c = x/(5 + x)$, where x is the molar ratio of Zr. The
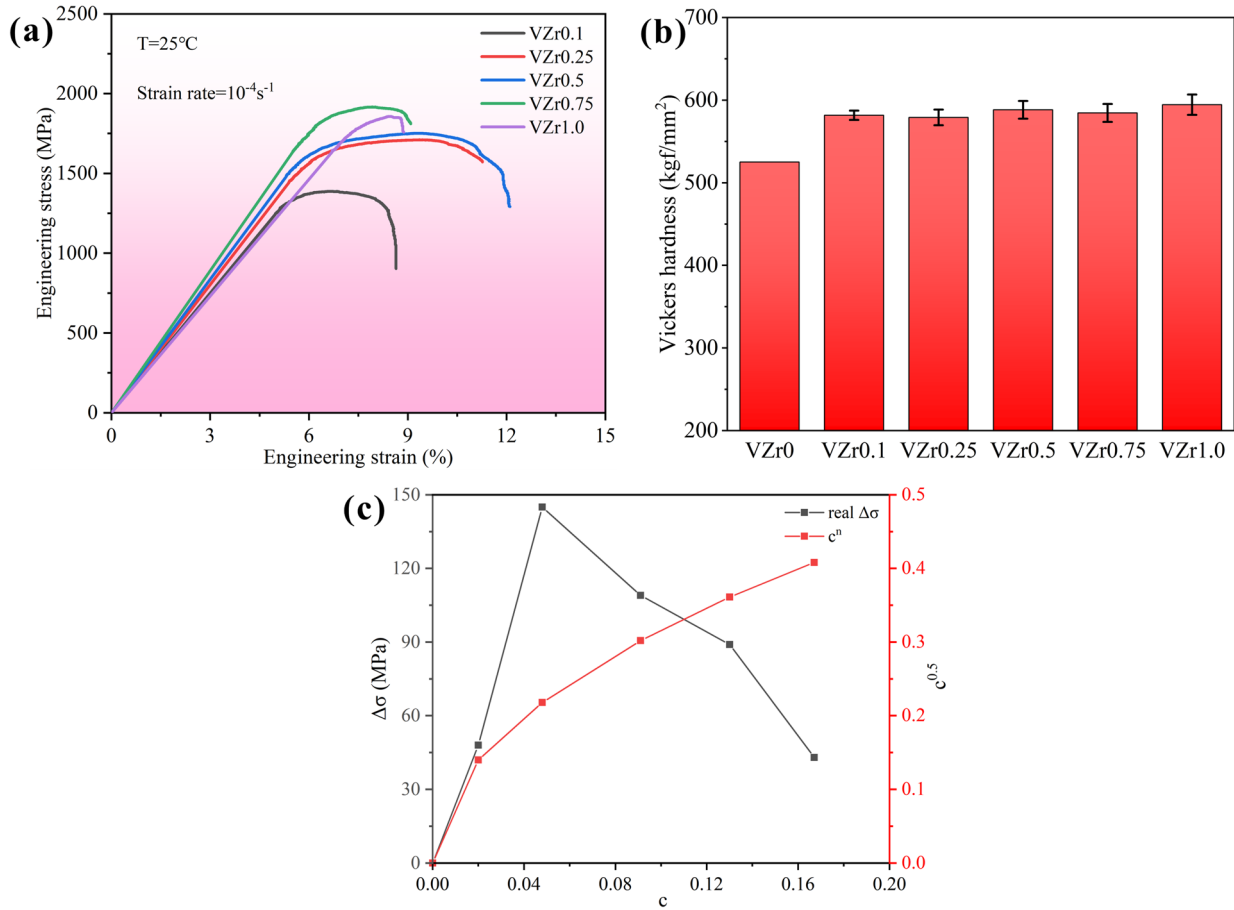
Figure 5: (a) Compressive stress–strain curves of the WNbMoTaVZr$_x$ RHEAs; (b) Vickers hardness data of the WNbMoTaVZr$_x$ RHEAs, as compared with the WNbMoTaV RHEA (VZr0); (c) c–$\Delta\sigma$ and c–c^n curves of the WNbMoTaVZr$_x$ RHEAs, where c increased with the increase of Zr content.

TABLE 5: The mechanical properties of the WNbMoTaVZr$_x$ RHEAs.

RHEA	σ_y (MPa)	σ_m (MPa)	ε_f (%)	Vicker hardness(kgf mm^{-2})
VZr0 [11]	1246	1270	1.7	525 [17]
VZr0.1	1294 ± 16	1422 ± 26	1.99 ± 0.20	582 ± 6
VZr0.25	1439 ± 25	1671 ± 37	3.79 ± 0.53	579 ± 9
VZr0.5	1548 ± 39	1788 ± 37	3.85 ± 0.31	588 ± 11
VZr0.75	1637 ± 8	1919 ± 28	2.63 ± 0.14	584 ± 11
VZr1.0	1680 ± 34	1913 ± 70	2.10 ± 0.45	595 ± 12

c–$\Delta\sigma$ and c–c^n curves of the WNbMoTaVZr$_x$ RHEAs are shown in Fig. 5(c). It can be seen that the experimental c–$\Delta\sigma$ curve is different from the calculated values (c–c^n curve), which can be divided into two different stages. With relative smaller Zr content, i.e., $x = 0.1$ (VZr0.1) and 0.25 (VZr0.25), the increasing trend for the yield strength is consistent with the calculated values, resulting from the solid solution strengthening effect. However, with the increase of Zr content ($x = 0.5$–1.0), the increasing trend for strength decreased. This may be due to the formation

of more BCC2 phase enriched with Zr and Nb elements. Previous studies have shown that for WNbMoTa-based RHEAs, the W and Ta-enriched dendrites are harder than the other regions with less W or Ta concentrations [19], while the BCC2 phase in interdendritic regions, enriched with Zr or Nb, could be softer than the dendrites. The increased volume fraction of soft BCC2 phase in these RHEAs may therefore weaken the solid solution strengthening effect [38–40], resulting in the smaller increase of yield strength. Such weakening effect could also be reasons for the small variation of hardness values of the RHEAs.

Besides the significant increase of strength and hardness, slightly increase of fracture strain (ε_f) of the WNbMoTaVZr$_x$ RHEAs was also observed, as compared with the WNbMoTaV RHEA (VZr0). And the largest average fracture strain of 3.85% was observed in the VZr0.5 RHEA (Table 5). The increase of the fracture strains of the RHEAs can be attributed to the increase of more Zr content and the resultant change of the microstructure. In order to give more insight into the deformation mechanisms of the WNbMoTaVZr$_x$ RHEAs, the deformation evolution of a typical VZr0.5 RHEA was examined using step-by-step
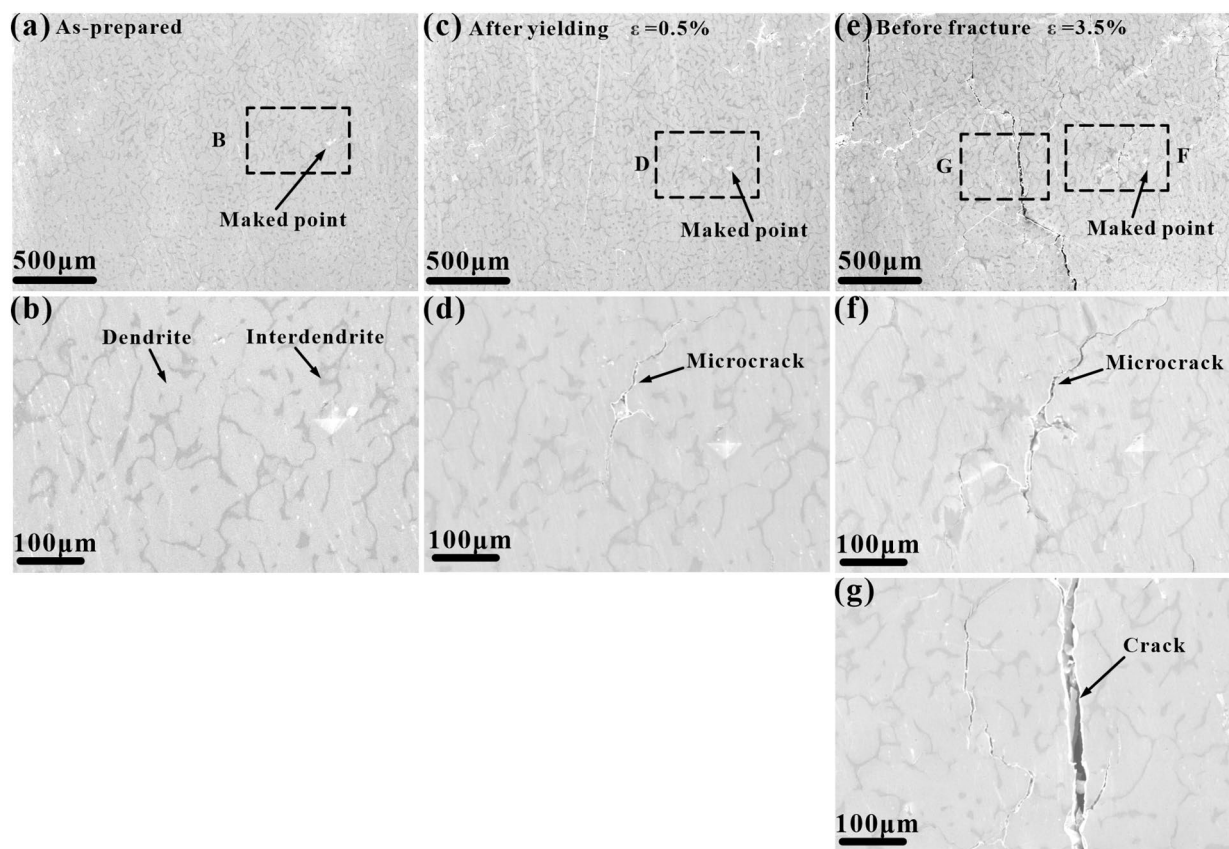
Figure 6: Deformation evolution of the typical Zr0.5 RHEA at three different states, i.e., as-prepared (a), after yielding (c) and before fracture (e), where (b, d, f and g) are the magnified regions of rectangles B, D, F and G, respectively.

observations. The SEM images of the specimens at different deformation stages, i.e., as-prepared, after yielding and before fracture, are shown in Fig. 6. In order to better characterize the evolution of the deformed specimens, a Vickers hardness indentation point was created as the mark point for surface observation. The formation of dendritic regions and interdendritic regions is indicated in Fig. 6(b). It can be seen that after yielding, microcracks were initiated at interdendritic regions [Fig. 6(d)]. With the addition of Zr, the distribution of Zr, V and Nb elements were more concentrated in the interdendritic regions, which are relatively softer than the W and Ta-riched dendrites [19]. Under applied loadings, the stress tends to concentrate at the interdendritic regions [6, 41]. Microcracks were therefore initiated in these interdendritic regions. The propagation of the microcracks was impeded by the relatively hard dendrites, and along the interdendritic regions, which could result in the improvement of the plasticity of WNbMoTaVZr$_x$ RHEAs. When loading proceeded to the strain of about 3.5% before fracture [Fig. 6(e)], the microcracks in Fig. 6(d) propagated continuously along the interdendritic regions [Fig. 6(f)]. On the other hand, during the evolution of plastic deformation and the severe lattice distortion effect, the stress may be concentrated to some

regions where the propagation of some other microcracks cannot be hindered by dendrites. These microcracks finally evolved to macroscopic cracks crossing the dendrites [Fig. 6(g)], causing the final failure of the specimen. Although limited enhancement of the plasticity of the RHEAs was observed, the present findings have shown that the addition of Zr can result in the formation of microstructures with hard dendrite and soft interdendritic regions. The tuning of the microstructures with different physical properties in RHEAs could be effective to further improve the plasticity in future.

The fracture morphology of the RHEAs is given in Fig. 7. The VZr0.1 RHEA shown mainly intergranular fracture morphology, where brittle fracture surface features such as river patterns were also observed. This is in line with the BCC phase structure with grain morphology [Fig. 2(a)], similar to the results of the parent WNbMoTaV RHEA. With increased Zr addition, the fracture mode of the VZr0.25 RHEA changed from intergranular fracture in VZr0.1 RHEA to transgranular fracture. A large amount of river patterns, with the indication of transgranular fracture surface features, was observed. This may result from the change of microstructure from the granular morphology to typical dendritic structure with the addition of
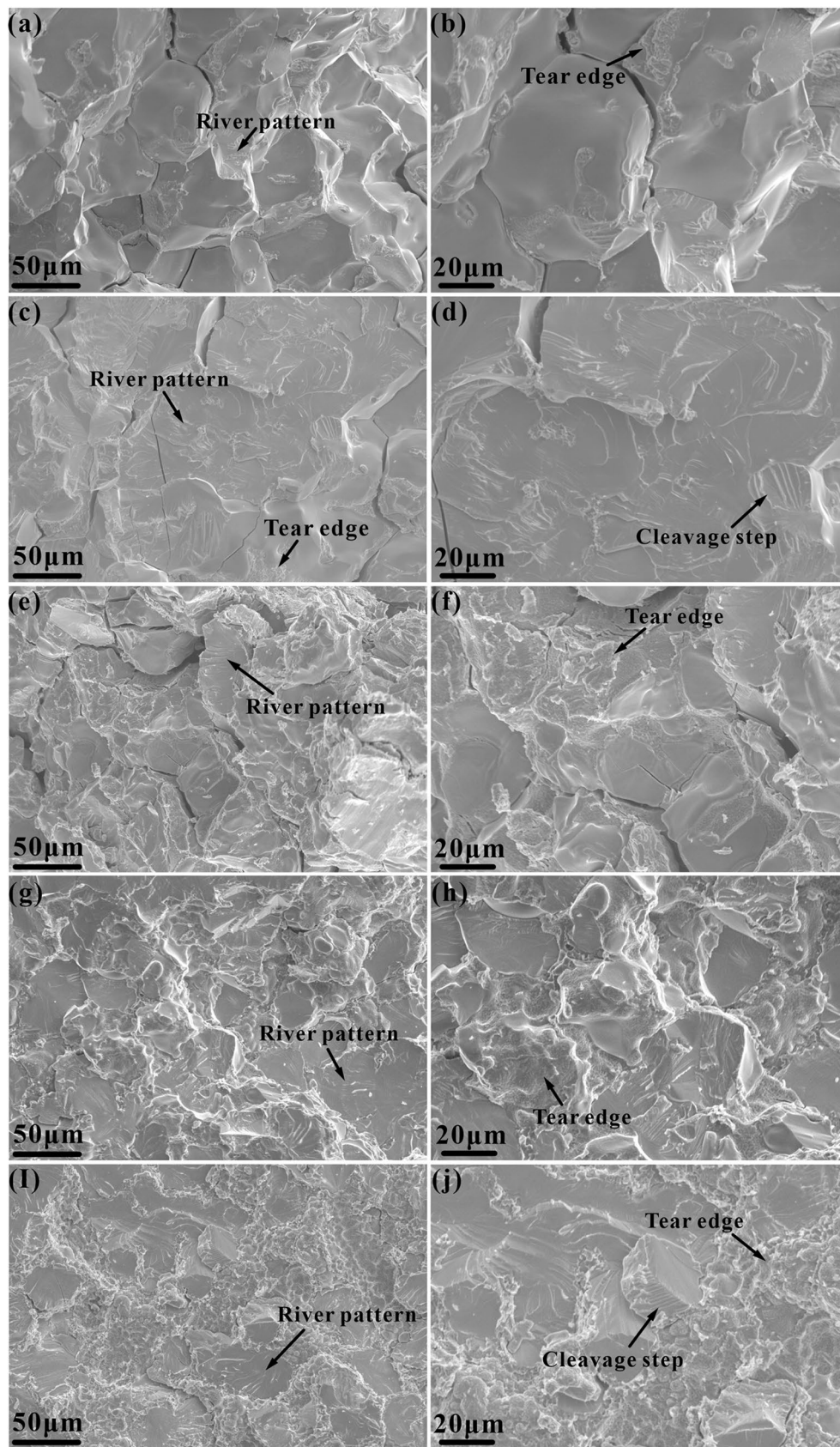
Figure 7: Fracture morphology of the VZr0.1 (a, b), VZr0.25 (c, d), VZr0.5 (e, f), VZr0.75 (g-h), and VZr1.0 (i-j) RHEAs at different magnifications.
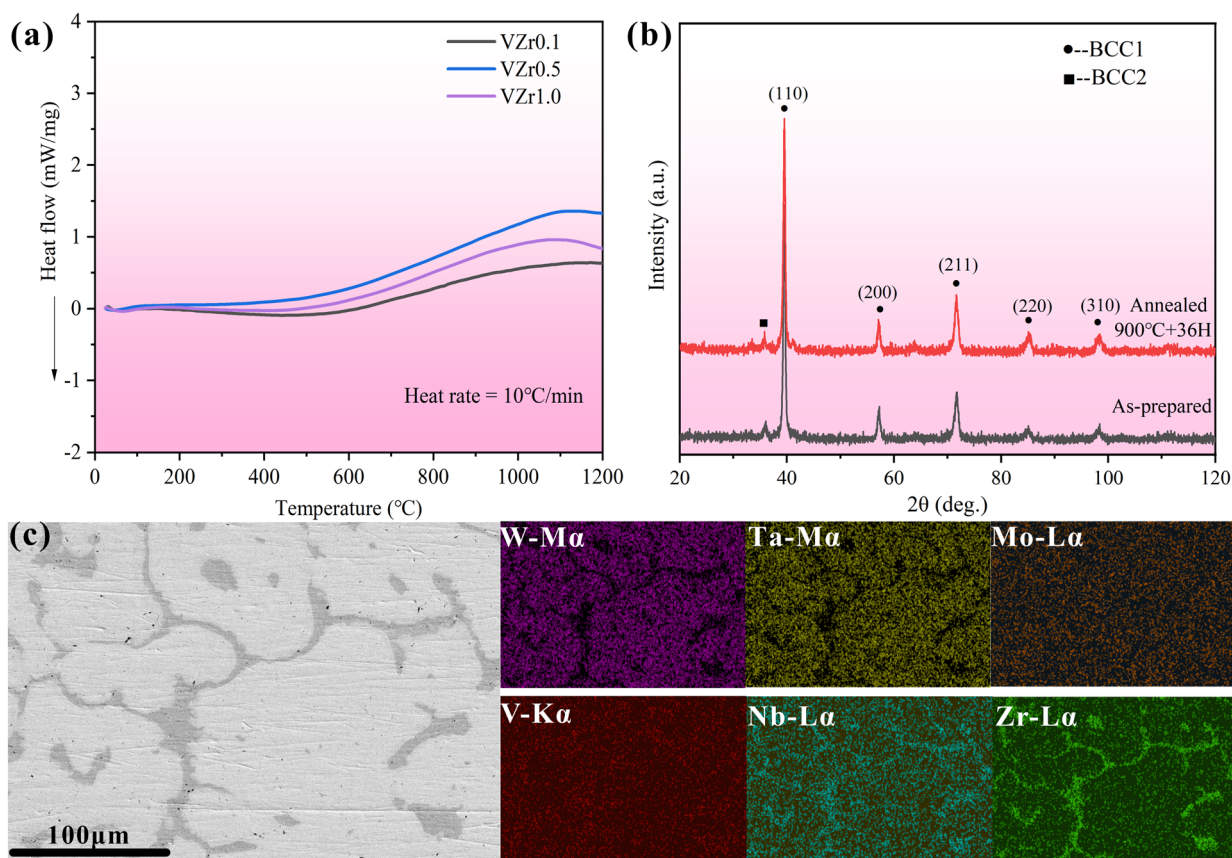
Figure 8: (a) DSC traces of three typical VZr0.1, VZr0.5 and VZr1.0 RHEAs from room temperature to 1200 °C; (b) XRD patterns of the VZr1.0 RHEA after annealing at 900 °C for 36 h, as compared with the as-prepared state; (c) SEM images of the microstructure of the annealed VZr1.0 RHEA, and the corresponding EDS mapping results.

Zr element. The change of the fracture mode should be responsible for the enhancement of the fracture strain in the VZr0.25 RHEA. However, with the further increase of Zr content in VZr0.5, VZr0.75 and VZr1.0 RHEAs, the fracture surface features changed significantly, where a large amount of tear edges coexisting with several river patterns were observed. The tear edges are usually formed due to the plastic deformation of local regions. Here, the tear edges may be formed due to the increased volume fraction of the BCC2 phase. As discussed before, the BCC2 phase enriched with Zr and Nb elements is relatively soft, which can accommodate more plastic strains at local regions. Based on the results in Fig. 6, microcracks were initiated and propagated along the interdendritic regions with the BCC2 phase. These regions should experience more severe plastic deformation than the hard dendrites enriched with W and Ta elements, resulting in the formation of tear edges. The observation of more tear edges in the RHEAs with increased BCC2 phase volume fraction has further confirmed such assertion. At the same time, the coexisted river patterns may result from the crossing of cracks from dendrite, as shown in Fig. 6(g). It should

be pointed out that although the macroscopic compressive plasticity was improved in the present RHEAs, the overall plasticity is still very limited when compared with other ductile HEAs and conventional alloys. It is interesting to find that the compressive plasticity decreased in the VZr0.75 and VZr1.0 RHEAs but with the observation of more tear edges when compared with the VZr0.5 RHEA. This may be due that the increased volume of the BCC2 phase can only accommodate the plastic strain at very localized regions, but cannot hinder the macroscopic fracture due to the "soft" phase nature. Further investigations on this phenomenon are still needed in future to give more insight in to the plastic deformation mechanisms.

Phase thermostability of the WNbMoTaVZr$_x$ RHEAs

In order to examine the phase thermostability of the WNbMoTaVZr$_x$ RHEAs, the differential scanning calorimetry (DSC) analyses of three VZr0.1, VZr0.5 and VZr1.0 RHEAs were heated to 1200 °C, and the DSC traces are shown in Fig. 8(a). It can be seen that no obvious exothermic/endothermic

TABLE 6: The room temperature property comparison of the WNbMoTa-X (X = Ti, V, Cr, Zr, Hf, Si, Re) RHEAs, where AM, ρ, σ_y, σ_m, ε_f, and SYS denote arc melting, density, yield strength, maximum compressive strength, fracture strain and specific yield strength, respectively.

Alloy	Preparing method	Phase	ρ (g cm^{-3})	σ_y (MPa)	σ_m (MPa)	ε_f (%)	SYS (MPa·cm^3 g^{-1})	Ref
WNbMoTaVZr$_{0.1}$	AM	2BCC	12.17	1294 ± 16	1422 ± 26	1.99 ± 0.20	106	This work
WNbMoTaVZr$_{0.25}$	AM	2BCC	11.95	1439 ± 25	1671 ± 37	3.79 ± 0.53	120	This work
WNbMoTaVZr$_{0.5}$	AM	2BCC	11.60	1548 ± 39	1788 ± 37	3.85 ± 0.31	133	This work
WNbMoTaVZr$_{0.75}$	AM	2BCC	11.30	1637 ± 8	1919 ± 28	2.63 ± 0.14	145	This work
WNbMoTaVZr$_{1.0}$	AM	2BCC	11.03	1680 ± 34	1913 ± 70	2.10 ± 0.45	152	This work
WNbMoTa	AM	BCC	13.63	1058	1211	1.5	78	[11]
WNbMoTaV	AM	BCC	12.34	1246	1270	1.7	101	[11]
WNbMoTaTi	AM	BCC	11.73	1343	2005	14.1	114	[6]
WNbMoTaVTi	AM	BCC	10.94	1515	2135	10.6	138	[6]
WNbMoTaTi$_0$	AM	BCC	13.62	996	1148	1.9	73	[19]
WNbMoTaTi$_{0.25}$	AM	BCC	13.06	1109	1197	2.5	85	[19]
WNbMoTaTi$_{0.5}$	AM	BCC	12.57	1211	1578	5.9	96	[19]
WNbMoTaTi$_{0.75}$	AM	BCC	12.13	1304	1593	8.4	108	[19]
WNbMoTaTi$_1$	AM	BCC	11.73	1455	1910	11.5	124	[19]
WNbMoTaCr	AM	Unknown	12.65	1056	1104	4.6	84	[20]
WNbMoTaZr	AM	Unknown	11.79	1480	1822	15.9	126	[20]
WNbMoTaV	AM	Unknown	12.34	1460	1520	8.8	118	[20]
WNbMoTaHf	AM	Unknown	13.49	1252	1252	5.7	93	[20]
WNbMoTaRe$_0$	AM	Unknown	13.62	1121 ± 8	1306 ± 13	6.22 ± 0.25	82	[20]
WNbMoTaRe$_{0.5}$	AM	BCC + particle	14.35	1147 ± 10	1465 ± 18	7.01 ± 0.30	80	[21]
WNbMoTaRe$_1$	AM	BCC + particle	14.95	1062 ± 15	1147 ± 10	4.22 ± 0.18	71	[21]

peak was observed for these RHEAs, which implies that the phase structure of the WNbMoTaVZr$_x$ RHEAs could be stable at high temperature till 1200 °C. Thereafter, annealing of the VZr1.0 RHEA with the largest volume fraction of the BCC2 phase was conducted at 900 °C for 36 h. The XRD result of the annealed VZr1.0 RHEA is given in Fig. 8(b). The main patterns indicate the formation of both BCC1 and BCC2 phases, which are the same with the results of as-prepared specimen, agreeing well with the DSC results. After annealing, the microstructure of the VZr1.0 RHEA is shown in Fig. 8(c). As compared with the microstructure of as-prepared VZr1.0 RHEA [Fig. 2(e)], it also showed a typical dendritic morphology and the elements distribution was also similar to the as-prepared specimens. The volume fraction of the BCC2 phase in annealed specimen was measured as 12.50%, which is slight smaller than the value of the as-prepared alloy (13.75%), without obvious coarsening or refining of the dendrites. The hardness of the annealed RHEA increased slightly from 595 ± 12 kgf mm^{-2} (as-prepared) to 612 ± 11 kgf mm^{-2}. This may be due to that the BCC2 phase was segregated and dissolved into the main BCC1 matrix during heat treatment, where slight decrease of the BCC2 volume fraction was also observed. The lattice distortion of the matrix may therefore be enhanced, resulting in the enhancement of hardness. It should be mentioned that although the present work suggests that the WNbMoTaVZr$_x$ RHEAs could have high phase thermostability at high temperature, further investigations under

harsher environment are needed in future in order to evaluate the high temperature performance of these RHEAs, for example, the creep behavior.

Discussion

Generally, an alloy with relative higher specific yield strength (SYS) tends to have better structural application potential for its low density and high yield strength [30]. Here, the SYS of present WNbMoTaVZr$_x$ RHEAs was compared with other WNbMoTa and WNbMoTaV derivative alloys. The preparing method, phase structure, mechanical properties of these alloys are also summarized in Table 6. It can be that the present WNbMoTaVZr$_x$ RHEAs have the highest strength value among the WNbMoTa and WNbMoTaV derivative alloys, especially the yield strength. More specifically, as shown in Fig. 9, those RHEAs were classified as low density-high SYS alloys and high density-low SYS alloys. The present WNbMoTaVZr$_x$ RHEAs tend to have lower density but with improved SYS with the addition of more Zr element. Especially, the VZr1.0 RHEA has the highest SYS. The improvement of the SYS is due to that the Zr element has larger atom radius, which brings in significant lattice distortion effect, and the increase of lattice distortion effect results in the improvement of strength. On the other hand, the Zr element has lower density than other elements, which can reduce the density of the WNbMoTaVZrx RHEAs. The increase
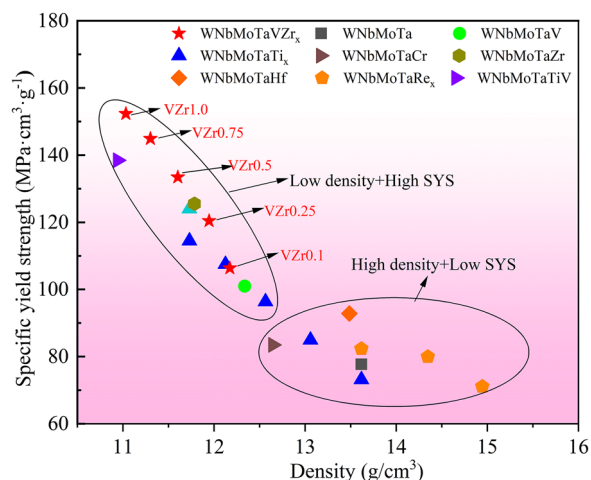
Figure 9: The comparison of the specific yield strength (SYS) and density of the present WNbMoTaVZrx RHEAs, as compared with other WNbMoTa [11], WNbMoTaV [11], WNbMoTaTix (x = 0, 0.25, 0.5, 0.75, 1.0), WNbMoTaVTi [6, 19], WNbMoTaZr [20], WNbMoTaHf [20], WNbMoTaRe (x = 0, 0.5, 1.0) [20, 21] and WNbMoTaCr [20] RHEAs.

of SYS and decrease of density could expand the structural application potential of the WNbMoTa-based RHEAs.

Furthermore, the Zr element has relatively low melting point, and tends to segregate into the interdendritic regions [8, 9, 19, 33, 42, 43]. The concentration of Zr element in the interdendritic regions can result in different physical properties between the dendrite and interdendritic regions, and therefore cause the formation of complex stress fields and improve the plasticity. The present work also demonstrated that the microcrack tends to initiate at interdendritic regions, and the propagation of cracks can be impeded by dendrites. This suggests that by designing dendritic microstructures with the addition of elements could be useful for further improving the plasticity of the WNbMoTa-based RHEAs and expanding their practical engineering applications. Based on the present findings, the addition of other elements with large atom radius and low density, such as Al and Ti, or the elements with relative lower melting point, such as Fe, Co, and Ni could be useful for the enhancing the comprehensive mechanical properties of RHEAs. Ni-based superalloys are usually used in heat engines, such as jet engines and power-generation turbines, which have high operation temperature (1160 °C to 1277 °C) [44, 45]. As compared with two typical Ni-based superalloys (Inconel 718 and Haynes 230), the present WNbMoTaVZr$_x$ RHEAs have higher SYS than Inconel 718 (about 148 MPa cm^3 g^{-1}), and the value is significantly higher than that of the Haynes 230 (about 45 MPa·cm^3·g^{-1}) [11]. More importantly, the present WNbMoTaVZr$_x$ RHEAs have melting points reaching 2551 °C, which is much larger than the melting points of Ni-based superalloys (around 1300 °C). The WNbMoTaVZr$_x$ RHEAs could therefore have

excellent high temperature mechanical properties than traditional Ni-based superalloys [11]. Combined with low density and high SYS, the WNbMoTaVZr$_x$ RHEAs could also have great potential for high temperature applications, and further investigations may be devoted to uncover the high temperature mechanical properties of such class of RHEAs.

Conclusions

In this work, a novel WNbMoTaVZr$_x$ RHEA system ($x = 0.1$, 0.25, 0.5, 0.75 and 1.0, noted as VZr0.1, VZr0.25, VZr0.5, VZr0.75 and VZr1.0, respectively) was designed and developed. The corresponding phase structure, microstructure, mechanical properties as well as plastic deformation behavior were investigated. The main findings of this work are summarized as follows:

(1) With relatively smaller Zr contents, the VZr0.1 RHEA has a grain morphology with refined grain sizes as compared with the parent WNbMoTaV RHEA, while typical dendritic structure appeared in other VZr0.25-VZr1.0 RHEAs. With the increase of Zr content, the distributions of Zr, V and Nb elements were more concentrated in interdendritic regions. Moreover, phase thermostability analysis based on EDS and annealing of typical RHEAs suggests that the phase structure of the WNbMoTaVZr$_x$ RHEAs could demonstrate good stability at elevated temperature.

(2) The WNbMoTaVZr$_x$ RHEAs have demonstrated significantly enhanced strength and hardness than the WNbMoTaV RHEA. The typical specimens exhibited the improvement of yield strength from 1246 to 1680 MPa, and the maximum strength from 1270 to 1919 MPa, respectively. The enhancement of the strength and hardness was attributed to the solid solution strengthening effect, resulting from the severe lattice distortion with the addition of relatively larger atom-sized Zr element. The plastic deformation behavior was examined by use of step-by-step observations, and fracture morphology was also investigated. The findings have shown that the strengthening effect, plastic deformation and the fracture behavior were also dependent on the formation of relatively soft BCC2 phase resulting from the addition of more Zr content.

(3) The WNbMoTaVZrx RHEAs demonstrated improved specific yield strength (SYS) with the increase of Zr content, and the VZr1.0 RHEA has the highest SYS which is larger than other WNbMoTa and WNbMoTaV derivative alloys, and typical Ni-based superalloys (Inconel 718 and Haynes 230). The WNbMoTaVZr$_x$ RHEAs could also have great potential for high temperature applications.

Materials and methods

The WNbMoTaVZr$_x$ RHEA ingots were prepared by arc melting under an argon atmosphere in a water-cooled copper crucible, from pure elements with purities larger than 99.9%. In order to ensure the homogeneity, each alloy ingot was flipped and re-melted for 12 times. The phase structure of the prepared RHEAs was identified by standard XRD analysis on a PANalytical X-Pert PRO MPD X-ray diffractometer (Panaco Corporation, Netherlands) with Cu-Kα radiation. The microstructure of the RHEAs was examined on an SU8020 (Hitachi, Japan) scanning electron microscope, and the distribution of the elements was inspected using an Energy Dispersive Spectrometer (EDS). Samples with dimensions of 3 mm × 3 mm × 6 mm were cut from the prepared ingots using the electrical discharge machining (EDM) for mechanical tests. TEM analysis were examined on a JEM-2100F (JEOL, Japan) transmission electron microscope. TEM specimens were cut from the ingots with 3 mm in diameter using electrical discharge machining (EDM), and then polished to 50 μm thickness discs using abrasive papers. They were further ion milled to electron transparency by a precision ion polishing system Gatan 691 (Gatan, USA). Compression tests were conducted on a universal Materials Testing Machine at an initial strain rate of 1×10^{-4} s^{-1}, and three specimens were tested for each condition. The micro hardness of the RHEAs was tested by a Vickers hardness tester under a load of 1 kgf and hold for 10 s. Six hardness data were collected and the average value was used for analysis. In order to the examine the deformation behavior of the RHEAs, the deformation evolution of a typical VZr0.5 RHEA was examined using step-by-step observations [46], and the deformed specimens were also inspected using SEM. In order to examine the phase thermostability of the WNbMoTaVZrx RHEAs, DSC analyses were conducted on an STA 449 F3 (Netzsch, Germany) under argon atmosphere with a heating rate of 10 °C min^{-1}, and the testing temperature ranged from 25 to 1200 °C. The typical VZr1.0 RHEA ingot was annealed at 900 °C for 36 h under an argon atmosphere with the heating rate of 10 °C min^{-1}, and then cooled in the furnace.

Author contributions

No applicable.

Funding

Data availability

The datasets generated during and/or analyzed during the current study are available from the corresponding author on reasonable request.

Code availability

No applicable.

Declarations

Conflict of interest The authors have no interest conflicts to declare in this article.

References

1. J.W. Yeh, S.K. Chen, S.J. Lin, J.Y. Gan, T.S. Chin, T.T. Shun, C.H. Tsau, S.Y. Chang, Nanostructured high-entropy alloys with multiple principal elements: novel alloy design concepts and outcomes. Adv. Eng. Mater. **6**(5), 299–303 (2004)

2. J.W. Yeh, Physical metallurgy of high-entropy alloys. JOM **67**(10), 2254–2261 (2015)

3. Y. Zhang, T.T. Zuo, Z. Tang, M.C. Gao, K.A. Dahmen, P.K. Liaw, Z.P. Lu, Microstructures and properties of high-entropy alloys. Prog. Mater. Sci. **61**, 1–93 (2014)

4. S. Ranganathan, Alloyed pleasures: Multimetallic cocktails. Curr. Sci. **85**(10), 1404–1406 (2003)

5. C. Xiang, H.M. Fu, Z.M. Zhang, E.H. Han, H.F. Zhang, J.Q. Wang, G.D. Hu, Effect of Cr content on microstructure and properties of Mo0.5VNbTiCrx high-entropy alloys. J. Alloys Compd. **818**, 153352 (2020)

6. Z.D. Han, N. Chen, S.F. Zhao, L.W. Fan, G.N. Yang, Y. Shao, K.F. Yao, Effect of Ti additions on mechanical properties of NbMoTaW and VNbMoTaW refractory high entropy alloys. Intermetallics **84**, 153–157 (2017)

7. É. Fazakas, V. Zadorozhnyy, L.K. Varga, A. Inoue, D.V. Louzguine-Luzgin, F. Tian, L. Vitos, Experimental and theoretical study of Ti20Zr20Hf20Nb20X20 (X=V or Cr) refractory high-entropy alloys. Int. J. Refract. Met. H **47**, 131–138 (2014)

8. M. Wang, Z. Ma, Z. Xu, X. Cheng, Microstructures and mechanical properties of HfNbTaTiZrW and HfNbTaTiZrMoW refractory high-entropy alloys. J. Alloys Compd. **803**, 778–785 (2019)

9. C.C. Juan, M.H. Tsai, C.W. Tsai, C.M. Lin, W.R. Wang, C.C. Yang, S.K. Chen, S.J. Lin, J.W. Yeh, Enhanced mechanical properties of HfMoTaTiZr and HfMoNbTaTiZr refractory high-entropy alloys. Intermetallics **62**, 76–83 (2015)

10. T.E. Whitfield, H.J. Stone, C.N. Jones, N.G. Jones, Microstructural degradation of the AlMo0.5NbTa0.5TiZr refractory metal high-entropy superalloy at elevated temperatures. Entropy **23**(1), 80 (2021)

11. O.N. Senkov, G.B. Wilks, J.M. Scott, D.B. Miracle, Mechanical properties of Nb25Mo25Ta25W25 and V20Nb20Mo20Ta20W20

refractory high entropy alloys. Intermetallics **19**(5), 698–706 (2011)

12. Y. Liu, Y. Zhang, H. Zhang, N. Wang, X. Chen, H. Zhang, Y. Li, Microstructure and mechanical properties of refractory HfMo0.5NbTiV0.5Six high-entropy composites. J. Alloys Compd. **694**, 869–876 (2017)

13. B. Gorr, F. Müller, M. Azim, H.-J. Christ, T. Müller, H. Chen, A. Kauffmann, M. Heilmaier, High-temperature oxidation behavior of refractory high-entropy alloys: effect of alloy composition. Oxid. Met. **88**(3–4), 339–349 (2017)

14. Q. Fang, Y. Chen, J. Li, Y. Liu, Y. Liu, Microstructure and mechanical properties of FeCoCrNiNbX high-entropy alloy coatings. Physica B **550**, 112–116 (2018)

15. Y.J. Hsu, W.C. Chiang, J.K. Wu, Corrosion behavior tion. Mater. Chem. Phys. **92**(1), 112–117 (2005)

16. Y. Chen, T. Duval, U. Hung, J. Yeh, H. Shih, Microstructure and electrochemical properties of high entropy alloys-a comparison with type-304 stainless steel. Corros. Sci. **47**(9), 2257–2279 (2005)

17. O.N. Senkov, G.B. Wilks, D.B. Miracle, C.P. Chuang, P.K. Liaw, Refractory high-entropy alloys. Intermetallics **18**(9), 1758–1765 (2010)

18. Y.C. Wu, Corrosion behavior of FeCoNiCrCux high-entropy alloys in 3.5% sodium chloride solution. Acta Metall. Sin. **55**(2), 171–180 (2018)

19. Z.D. Han, H.W. Luan, X. Liu, N. Chen, X.Y. Li, Y. Shao, K.F. Yao, Microstructures and mechanical properties of TixNbMoTaW refractory high-entropy alloys. Mater. Sci. Eng. A **712**, 380–385 (2018)

20. Y. Tong, L. Bai, X. Liang, Y. Chen, Z. Zhang, J. Liu, Y. Li, Y. Hu, Influence of alloying elements on mechanical and electronic properties of NbMoTaWX (X= Cr, Zr, V, Hf and Re) refractory high entropy alloys. Intermetallics **126**, 106928 (2020)

21. J. Zhang, Y. Hu, Q. Wei, Y. Xiao, P. Chen, G. Luo, Q. Shen, Microstructure and mechanical properties of RexNbMoTaW high-entropy alloys prepared by arc melting using metal powders. J. Alloys Compd. **827**, 154301 (2020)

22. J. Chen, P. Niu, Y. Liu, Y. Lu, X. Wang, Y. Peng, J. Liu, Effect of Zr content on microstructure and mechanical properties of AlCoCrFeNi high entropy alloy. Mater. Des. **94**, 39–44 (2016)

23. S.S.M. Pauzi, W. Darham, R. Ramli, M. Harun, M.K. Talari, Effect of Zr addition on microstructure and properties of FeCrNiMnCoZr$_x$ and Al0.5FeCrNiMnCoZr$_x$ high entropy alloys. Trans. Indian. Inst. Met. **66**(4), 305–308 (2013)

24. Y. Zhang, Y.J. Zhou, J.P. Lin, G.L. Chen, P.K. Liaw, Solid-solution phase formation rules for multi-component alloys. Adv. Eng. Mater. **10**(6), 534–538 (2008)

25. A. Takeuchi, A. Inoue, Classification of bulk metallic glasses by atomic size difference, heat of mixing and period of constituent elements and its application to characterization of the main alloying element. Mater. Trans. **46**(12), 2817–2829 (2005)

26. S. Guo, C. Ng, J. Lu, C.T. Liu, Effect of valence electron concentration on stability of fcc or bcc phase in high entropy alloys. J. Appl. Phys. **109**(10), 103505 (2011)

27. X. Yang, Y. Zhang, Prediction of high-entropy stabilized solid-solution in multi-component alloys. Mater. Chem. Phys. **132**(2–3), 233–238 (2012)

28. C.J. Tong, Y.L. Chen, J.W. Yeh, S.J. Lin, S.K. Chen, T.T. Shun, C.H. Tsau, S.Y. Chang, Microstructure characterization of Alx-CoCrCuFeNi high-entropy alloy system with multiprincipal elements. Metall. Mater. Trans. A **36**(4), 881–893 (2005)

29. K.Y. Tsai, M.H. Tsai, J.W. Yeh, Sluggish diffusion in Co–Cr–Fe–Mn–Ni high-entropy alloys. Acta Mater. **61**(13), 4887–4897 (2013)

30. Z.Q. Xu, Z.L. Ma, M. Wang, Y.W. Chen, Y.D. Tan, X.W. Cheng, Design of novel low-density refractory high entropy alloys for high-temperature applications. Mater. Sci. Eng. A **755**, 318–322 (2019)

31. Y. Guo, H. Wang, Q. Liu, Microstructure evolution and strengthening mechanism of laser-cladding MoFeCrTiWAlNb refractory high-entropy alloy coatings. J. Alloys Compd. **834**, 155147 (2020)

32. D. Patel, M.D. Richardson, B. Jim, S. Akhmadaliev, R. Goodall, A.S. Gandy, Radiation damage tolerance of a novel metastable refractory high entropy alloy V2.5Cr1.2WMoCo0.04. J. Nucl. Mater. **531**, 152005 (2020)

33. Z. Sun, X. Li, Z. Wang, Microstructure and mechanical properties of low activation Fe–Ti–Cr–V–W multi-principal element alloys. J. Nucl. Mater. **533**, 152078 (2020)

34. W. Zhang, P.K. Liaw, Y. Zhang, A Novel low-activation VCrFe-TaxWx (x = 0.1, 0.2, 0.3, 0.4, and 1) high-entropy alloys with excellent heat-softening resistance. Entropy **20**(12), 951 (2018)

35. S.P. Wang, J. Xu, TiZrNbTaMo high-entropy alloy designed for orthopedic implants: as-cast microstructure and mechanical properties. Mater. Sci. Eng. C **73**, 80–89 (2017)

36. H. Zhang, L. Zhang, X. Liu, Q. Chen, Y. Xu, Effect of Zr addition on the microstructure and mechanical properties of CoCrFeNiMn high-entropy alloy synthesized by spark plasma sintering. Entropy **20**(11), 810 (2018)

37. S. Gao, T. Kong, M. Zhang, X. Chen, Y. Sui, Y. Ren, J. Qi, F. Wei, Y. He, Q. Meng, Z. Sun, Effects of titanium addition on microstructure and mechanical properties of CrFeNiTi x (x = 0.2 0.6) compositionally complex alloys. J. Mater. Res. **34**, 819–828 (2019)

38. D.J.M. King, S.T.Y. Cheung, S.A. Humphry-Baker, C. Parkin, A. Couet, M.B. Cortie, G.R. Lumpkin, S.C. Middleburgh, A.J. Knowles, High temperature, low neutron cross-section high-entropy alloys in the Nb-Ti-V-Zr system. Acta Mater. **166**, 435–446 (2019)

39. L. Wang, L. Wang, Y. Tang, L. Luo, L. Luo, Y. Su, J. Guo, H. Fu, Microstructure and mechanical properties of CoCrFeNiW high entropy alloys reinforced by μ phase particles. J. Alloys Compd. **843**, 155997 (2020)

40. O.N. Senkov, J. Gild, T.M. Butler, Microstructure, mechanical properties and oxidation behavior of NbTaTi and NbTaZr refractory alloys. J. Alloys Compd. **862**, 158003 (2021)

41. S.H. Chen, J.Y. Wang, L. Xia, Y.C. Wu, Deformation behavior of bulk metallic glasses and high entropy alloys under complex stress fields: a review. Entropy **21**(1), 54 (2019)

42. M. Pole, M. Sadeghilaridjani, J. Shittu, A. Ayyagari, S. Mukherjee, High temperature wear behavior of refractory high entropy alloys based on 4-5-6 elemental palette. J. Alloys Compd. **843**, 156004 (2020)

43. Z. Niu, J. Xu, T. Wang, N. Wang, Z. Han, Y. Wang, Microstructure, mechanical properties and corrosion resistance of CoCrFeNiW (x = 0, 0.2, 0.5) high entropy alloys. Intermetallics **112**, 106550 (2019)

44. T.M. Pollock, S. Tin, Nickel-based superalloys for advanced turbine engines: chemistry, microstructure and properties. J. Propul. Power **22**(2), 361–374 (2006)

45. J. Chen, X. Zhou, W. Wang, B. Liu, Y. Lv, W. Yang, D. Xu, Y. Liu, A review on fundamental of high entropy alloys with promising high-temperature properties. J. Alloys Compd. **760**, 15–30 (2018)

46. S.H. Chen, K.C. Chan, F.F. Wu, L. Xia, Pronounced energy absorption capacity of cellular bulk metallic glasses. Appl. Phys. Lett. **104**, 111907 (2014)